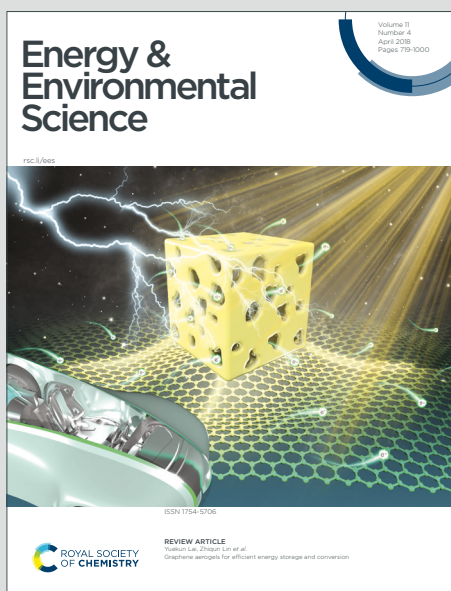


Energy & Environmental Science

Accepted Manuscript

This article can be cited before page numbers have been issued, to do this please use: J. G. Son, H. Koo, W. J. Lee, D. Kim, S. Park, J. Roe, J. Seo, J. M. Ha, H. Lee, W. Lee, H. Y. Woo, S. Cho, D. S. Kim, S. Shin and J. Y. Kim, *Energy Environ. Sci.*, 2026, DOI: 10.1039/D5EE07006F.



This is an Accepted Manuscript, which has been through the Royal Society of Chemistry peer review process and has been accepted for publication.

Accepted Manuscripts are published online shortly after acceptance, before technical editing, formatting and proof reading. Using this free service, authors can make their results available to the community, in citable form, before we publish the edited article. We will replace this Accepted Manuscript with the edited and formatted Advance Article as soon as it is available.

You can find more information about Accepted Manuscripts in the [Information for Authors](#).

Please note that technical editing may introduce minor changes to the text and/or graphics, which may alter content. The journal's standard [Terms & Conditions](#) and the [Ethical guidelines](#) still apply. In no event shall the Royal Society of Chemistry be held responsible for any errors or omissions in this Accepted Manuscript or any consequences arising from the use of any information it contains.

Broader context

The transition toward a carbon-neutral society demands technologies capable of producing both renewable electricity and sustainable fuels from sunlight. While perovskite solar cells (PSCs) have reached efficiencies rivaling silicon, extending their functionality toward solar-driven fuel generation remains a key challenge. This study introduces a molecular-engineering approach that stabilizes the buried interfaces of perovskite/organic tandem devices through controlled deprotonation of self-assembled monolayers (SAMs). The resulting mixed-state 2PACz-K forms robust chemical coordination with conductive oxides, enabling both efficient charge extraction and long-term durability. Beyond advancing high-efficiency tandem photovoltaics, this interfacial strategy is extended to photoelectrochemical cell (PEC) systems, leading to the first transparent, metal-free tandem photocathode capable of stable operation in aqueous media. By unifying the design principles of photovoltaic and photoelectrochemical platforms, this work demonstrates how molecular-level interface control can accelerate the integration of solar electricity and fuel production—offering a scalable, low-cost pathway toward sustainable solar-energy conversion and storage.



Deprotonated Self-Assembled Molecules as Robust Hole-Selective Layers for Perovskite/Organic Tandem Solar Cells and Photocathodes

Jung Geon Son^{‡a}, Ha-eun Koo^{‡a}, Woojin Lee^{‡a}, Dongyoung Kim^a, Sujung Park^b, Jina Roe^a, Jongdeuk Seo^a, Jung Min Ha^c, Heunjeong Lee^b, Wangyeon Lee^a, Han Young Woo^c, Shinuk Cho^b, Dong Suk Kim^{*ad}, Seung-Jae Shin^{*a}, and Jin Young Kim^{*ad}

^a School of Energy and Chemical Engineering, Ulsan National Institute of Science and Technology (UNIST), UNIST-gil 50, Ulsan 44919, Republic of Korea

^b Department of Semiconductor Physics and EHSRC, University of Ulsan, Ulsan 44610, Republic of Korea

^c Department of Chemistry, Korea University, Seoul 02841, Republic of Korea

^d Graduate School of Carbon Neutrality, Ulsan National Institute of Science and Technology (UNIST), UNIST-gil 50, Ulsan 44919, Republic of Korea

[‡]These authors equally contributed to this work.



Abstract

Self-assembled monolayer (SAM)-based hole-selective layers (HSLs) offer a promising route to defect-passivated and energy-aligned interfaces in perovskite organic tandem solar cells (POTSCs). However, their practical implementation remains hindered by weak anchoring to transparent conductive oxides (TCOs), leading to desorption during perovskite deposition and poor interfacial durability under polar solvent exposure. Here, we present a chemical interfacial stabilization strategy in which potassium carbonate (K_2CO_3) mediates the controlled deprotonation of [2-(9*H*-carbazol-9-yl)ethyl]phosphonic acid (2PACz), forming mixed mono- and di-deprotonated species (2PACz-K) that bind strongly to indium tin oxide (ITO). The resulting SAM exhibits superior solvent resistance, improved energy-level alignment, and enhanced buried interface quality. POTSCs incorporating 2PACz-K achieve 25.10% power conversion efficiency (PCE) with a high open-circuit voltage (V_{OC}) of 2.230 V, while retaining 80% of their initial PCE after 220 h of maximum power point (MPP) tracking under simulated 1-sun illumination. Beyond photovoltaics, the robust 2PACz-K interface is further integrated into a perovskite/organic tandem photocathode (POT-PEC), representing the first transparent, metal-free tandem PEC architecture capable of stable operation in aqueous electrolyte, delivering a photovoltage (V_{ph}) of 2.16 V and achieving solar-to-hydrogen (STH) conversion efficiency of 7.7%. This work establishes a versatile interfacial design paradigm that bridges photovoltaic and photoelectrochemical energy conversion.

Keywords: Self-assembled monolayers, Interfacial stability, Solvent-resistant hole-selective layers, Perovskite/organic tandem solar cells, Photoelectrochemical water splitting



Introduction

The escalating global demand for sustainable energy highlights the urgent need for carbon-neutral technologies that can deliver both electricity and renewable fuels. Solar photovoltaics (PVs) and photoelectrochemical cells (PECs) represent two of the most promising strategies for harvesting sunlight and converting it into usable energy forms—electricity and hydrogen. However, their independent device architecture and stability constraints hinder integration into unified solar-energy platforms. In this context, perovskite/organic tandem architecture offers a compelling opportunity to bridge PV and PEC functionalities, combining the high efficiency and bandgap tunability of perovskite absorbers with the hydrophobicity and spectral complementarity of organic semiconductors. Such hybrid tandem designs are not only well suited for efficient solar-to-electricity conversion but provide a promising foundation for solar-driven hydrogen production.

Single-junction perovskite solar cells (PSCs) have achieved impressive power conversion efficiencies (PCEs) exceeding 27.0% within just over a decade, underscoring the rapid progress of perovskite photovoltaics.¹ Despite this achievement, further efficiency gains are fundamentally constrained by the Shockley-Queisser limit (S-Q limit) (33.7%) for single-junction devices.² To overcome this limitation, tandem architecture has emerged as a promising approach to more efficiently utilize the solar spectrum and reduce thermalization losses.³ The perovskite-based tandem architectures have been extensively investigated, and we summarized the representative architectures and performance in Table S1. Among various designs, monolithic perovskite/organic tandem solar cells (POTSCs) have attracted increasing attention owing to their use of orthogonal solvents,⁴ highly tunable bandgaps,^{5,6} and superior stability compared to all-perovskite tandems that often suffer from rapid Sn²⁺/Sn⁴⁺ oxidation.^{7,8} Moreover, the hydrophobic organic layers provide an additional functional advantage—inherent resistance to aqueous environments—rendering POTSCs particularly suitable as a bridge between PV and PEC applications.⁹ From a PEC perspective, the optical transparency is particularly advantageous because a transparent photocathode can be serially combined with a complementary light absorber/photoanode to increase the overall photovoltage, providing a bias-free solar-fuel system.

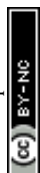
Despite these advancements, the performance and scalability of wide-bandgap (WBG) perovskite solar cells (PSCs) remain limited by significant open-circuit voltage (V_{OC}) losses. These losses originate primarily from non-radiative recombination at imperfect buried interfaces,^{10,11} energy-level mismatches,^{12,13} and interfacial instability arising from chemical



interactions with polar solvents during perovskite processing.^{14,15} Among various strategies to mitigate these issues, the design of robust hole-selective layers (HSLs) has emerged as a crucial determinant of both interfacial energetic and perovskite film formation. Recent efforts employing self-assembled monolayers (SAMs) have demonstrated their potential to provide molecularly defined interfaces with tunable surface dipoles and reduced defect densities.^{10,16,17} However, their practical use in perovskite processing remains challenged by incomplete coverage and weak binding to transparent conductive oxides (TCOs) such as indium tin oxide (ITO) and fluorine-doped tin oxide (FTO), often resulting in desorption or morphological inhomogeneity under polar solvents.^{3,14,15} Consequently, developing chemically stable, solvent-resistant SAM-based HSLs is essential for advancing perovskite/organic tandem platforms and enabling their extension toward photoelectrochemical operation.

Herein, we introduce a chemical interfacial engineering strategy that stabilizes SAMs through potassium carbonate (K_2CO_3)-mediated deprotonation of [2-(9*H*-carbazol-9-yl)ethyl]phosphonic acid (2PACz). This process generates a mixed population of mono- and di-deprotonated species (2PACz⁻ and 2PACz²⁻), collectively referred to as 2PACz-K, which exhibit stronger binding affinity to ITO surfaces and enhanced chemical resilience against polar solvents. The resulting SAM forms a uniform, solvent-resistant HSL that maintains interfacial integrity during perovskite deposition and promotes improved crystallinity and energetics of the overlying WBG perovskite film. Device incorporating 2PACz-K achieved a PCE of 18.25% in WBG PSCs and 25.10% in POTSCs, accompanied by reduced hysteresis and enhanced operational stability. Moreover, leveraging its intrinsic chemical robustness and superior V_{OC} , the 2PACz-K interface was further extended to a transparent, metal-free perovskite organic tandem photocathode (POT-PEC) for solar to hydrogen conversion, achieving a photovoltage (V_{ph}) of 2.16 V and delivering solar-to-hydrogen (STH) conversion efficiency of 7.7%. These results establish 2PACz-K as a versatile interfacial material that bridges high-efficiency photovoltaics and durable solar-driven hydrogen conversion.

Results and Discussion



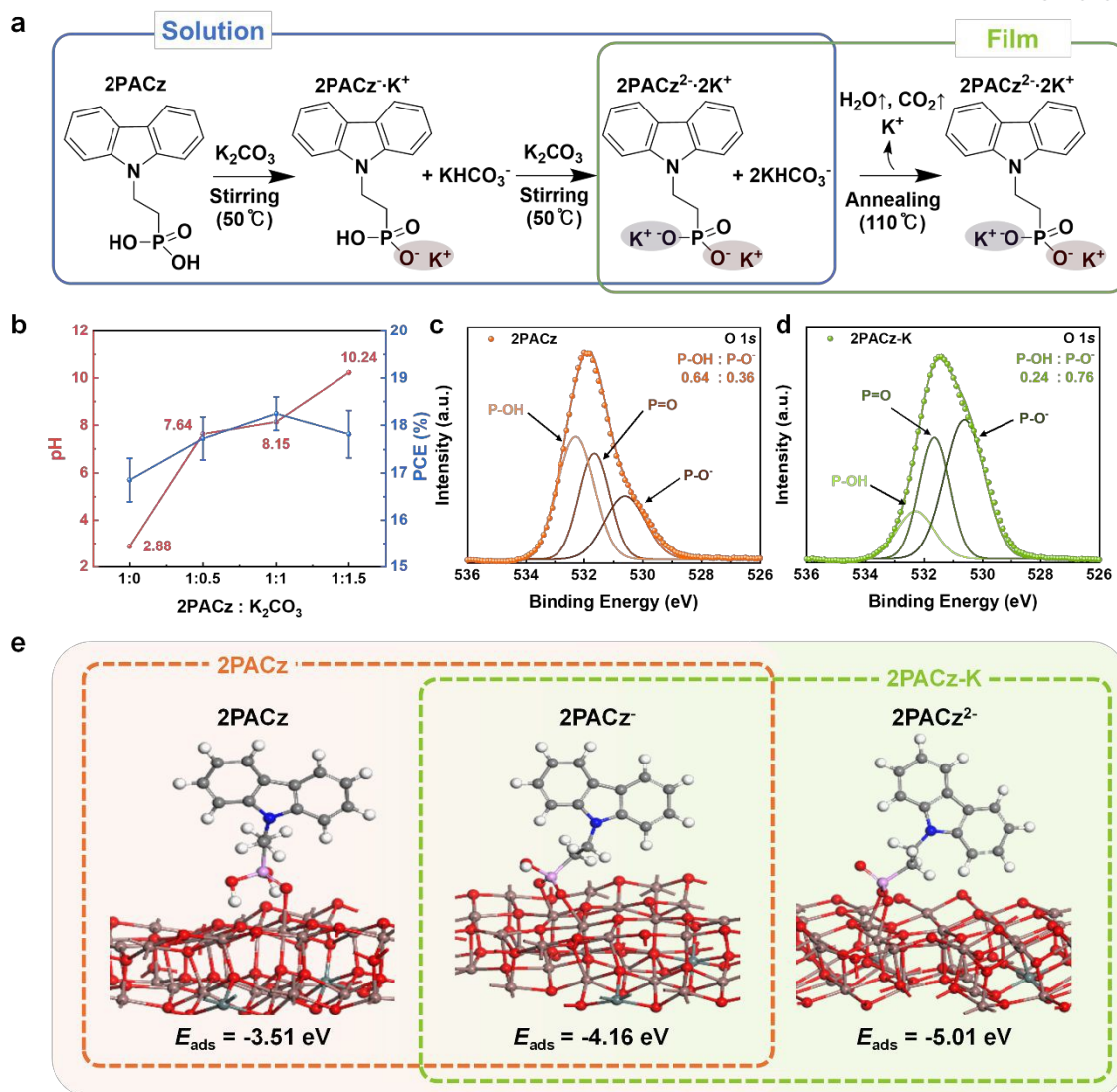


Figure 1. (a) Schematic illustration of stepwise deprotonation of 2PACz mixing with K_2CO_3 (1:1 molar ratio). (b) pH values of mixed 2PACz: K_2CO_3 solutions and the corresponding PCEs of WBG PSCs. (c-d) O 1s XPS spectra of 2PACz and 2PACz-K on glass substrates. (e) DFT-calculated adsorption energy (E_{ads}) of fully protonated 2PACz, mono-deprotonated 2PACz (2PACz⁻), and di-deprotonated 2PACz (2PACz²⁻) on the ITO surface.

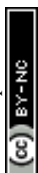
To elucidate K_2CO_3 mediates the deprotonation of 2PACz and strengthens its binding to the ITO surface, we first established the stepwise deprotonation pathway illustrated in **Figure 1a**. Upon addition of K_2CO_3 , the phosphonic acid moiety of 2PACz undergoes sequential deprotonation upon the addition of K_2CO_3 , forming mono- (2PACz⁻) and di-deprotonated (2PACz²⁻) species, collectively denoted as 2PACz-K. The process is accompanied by the release of CO_2 and H_2O , confirming the acid-base neutralization mechanism.



The deprotonation behavior was experimentally verified through pH titration of ethanolic 2PACz solutions at varying 2PACz:K₂CO₃ molar ratios (1:0.5, 1:1, 1:1.5), as shown in Figures 1b and S1. The measured pH increased from 2.88 for pristine 2PACz to 8.15 at a 1:1 molar ratio. Based on these values and the literature-reported $pK_{a1} = 2.5$ and $pK_{a2} = 8.5$ for phosphonic acids,^{18,19} the relative populations of the protonated species were estimated using standard diprotic equilibrium expressions (Supplementary Note 1). The calculation shows that in ethanolic 2PACz solutions, 2PACz⁻ is the dominant form (~71%) with only a minor fraction of the fully protonated 2PACz (~29%). Whereas in the presence of K₂CO₃ at 1:1 molar ratio, 2PACz²⁻ emerges as a significant component (~31%) while 2PACz⁻ remains predominant (~69%) (Table S2). These results confirm that K₂CO₃ induces partial but controlled deprotonation of 2PACz, leading to a mixed mono- and di-deprotonated state consistent with the formation of 2PACz-K.

X-ray photoelectron spectroscopy (XPS) provided further confirmation of this deprotonation state in this film. As presented in Figure 1c-d and Table S3, the O 1s XPS spectra of 2PACz and 2PACz-K films spin-coated on glass revealed a distinct shift toward higher P-O⁻ content in 2PACz-K (0.76 vs. 0.36), reflecting a greater proportion of deprotonated species capable of forming P-O-M (M = In/Sn) coordination with the ITO surface. To quantitatively assess the impact of this deprotonation on interfacial binding, density functional theory (DFT) calculations (Figure 1e and Supplementary Note 2) were performed,²⁰ showing that the adsorption energy (E_{ads}) becomes increasingly favorable with the degree of deprotonation: -3.51 eV for fully protonated 2PACz, -4.16 eV for 2PACz⁻, and -5.01 eV for 2PACz²⁻. Notably, this enhanced binding does not rely on a dehydration-driven condensation process that has been commonly proposed for protonated phosphonic-acid-based SAMs on oxide surfaces.^{21,22} While residual P-OH groups may, in principle, participate in hydroxyl-mediated condensation under certain surface conditions, K₂CO₃-mediated deprotonation fundamentally alters the dominant anchoring pathway by converting neutral P-OH groups into negatively charged P-O⁻ species. This charge-state transition enables direct ionic/coordinative interactions with In³⁺ and Sn⁴⁺ cations exposed at the ITO surface, consistent with the systematically increased adsorption energies observed in DFT calculations. As a result, interfacial stabilization in 2PACz-K is governed primarily by charge-assisted coordination rather than by conventional condensation pathways.

Taken together, these results confirm that K₂CO₃ treatment drives partial deprotonation of 2PACz, leading to the coexistence of 2PACz⁻ and 2PACz²⁻ species that bind more strongly ITO



surfaces. The resulting 2PACz-K layer is therefore chemically anchored through mixed P-O-M coordination, providing a robust foundation for subsequent solvent processing and perovskite film growth.

View Article Online
DOI: 10.1039/D5EE07006F

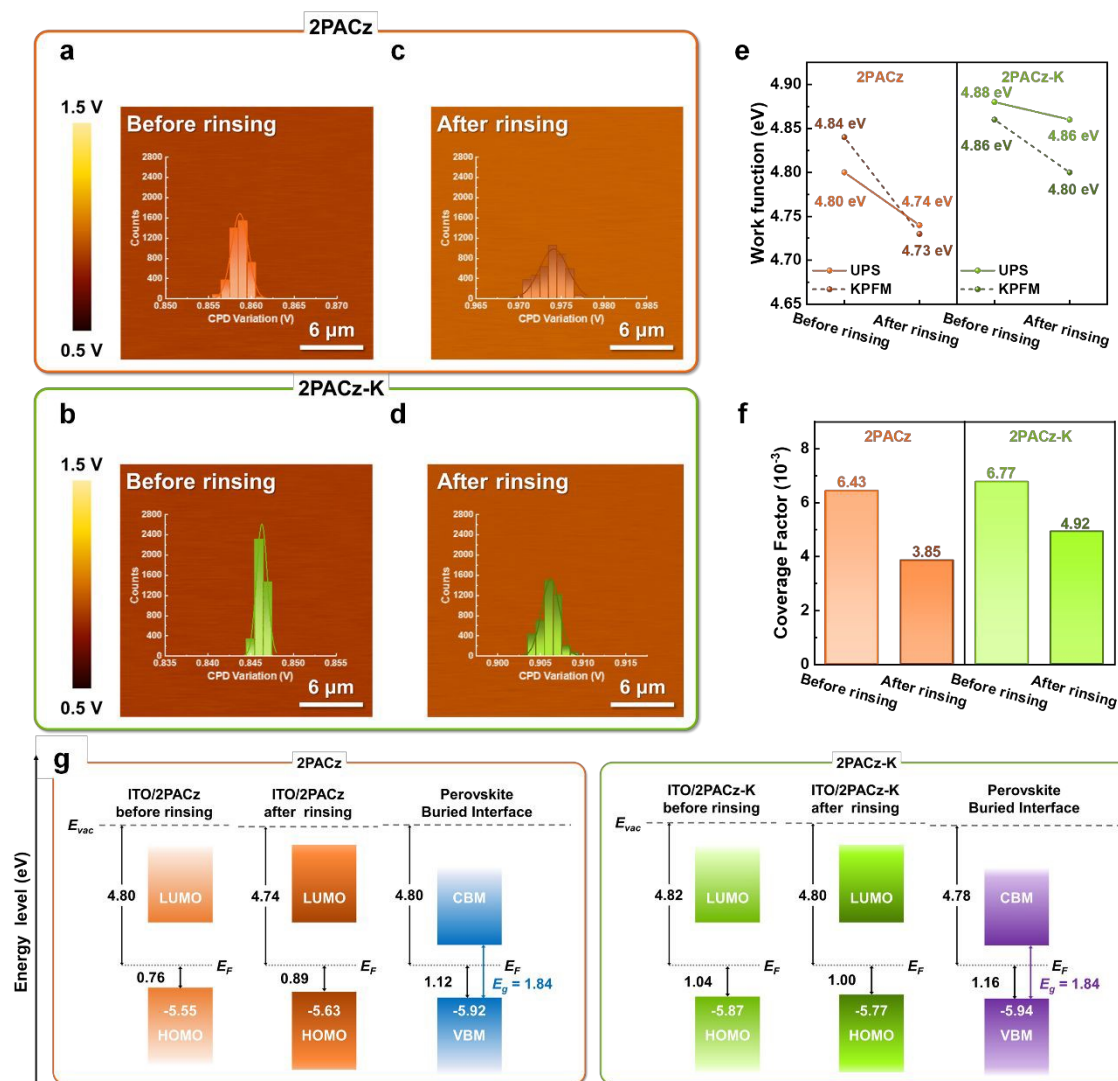


Figure 2. (a-d) KPFM images and corresponding Gaussian fitting curves of ITO/HSLs before and after DMF rinsing. (e) Comparison of work function of ITO/HSLs before and after DMF rinsing measured by UPS and KPFM. (f) Coverage factors of ITO/HSLs before and after DMF rinsing. (g) Energy level diagrams of ITO/HSLs and perovskite buried interfaces.

To further investigate the impact of the adsorption energy on the anchoring stability of HSLs, Kelvin probe force microscopy (KPFM) measurements were conducted to assess the surface potential of ITO/HSLs before and after rinsing with dimethylformamide (DMF). Since DMF is the primary solvent used during perovskite deposition, rinsing experiments were employed



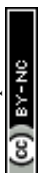
as a proxy to mimic solvent exposure and assess HSL robustness under relevant processing conditions. Before DMF rinsing, ITO/2PACz-K exhibited a lower contact potential difference (CPD) with a narrower distribution compared to ITO/2PACz (Table S4), indicating a deeper work function (WF) and improved microscopic uniformity in electronic properties (Figure 2a-b).²³

After DMF rinsing, the CPD of ITO/2PACz significantly decreased and showed a broader distribution (Figure 2c), closely resembling that of bare ITO (Figure S2), suggesting that a substantial portion of the SAM was removed.¹⁵ In contrast, ITO/2PACz-K maintained a relatively stable CPD profile post-rinsing (Figure 2d), confirming that the deprotonated species in 2PACz-K remain anchored on the ITO surface and maintain their electronic uniformity. Ultraviolet photoelectron spectroscopy (UPS) corroborated these observations, with WF values after DMF rinsing consistent with the KPFM results (Figures S3 and 2e). The deeper WF of ITO/2PACz-K relative to ITO/2PACz implies more compact molecular packing and reduced interfacial disorder.²⁴

To further assess the surface coverage and chemical integrity of the SAMs, XPS was performed before and after DMF exposure. The relative intensity ratio of C 1s and In 3d peaks (Figures S4-S5 and Table S5) revealed that 2PACz-K maintained higher coverage on ITO even after rinsing, while 2PACz films exhibited significant desorption (Figure 2f).³ This stability is consistent with the deprotonated species identified by DFT calculations, supporting the formation of a chemically robust SAMs on ITO.

Taken together, the KPFM, UPS, and XPS results indicate that the WF increased induced by K₂CO₃ treatment—and its subsequent decrease after DMF rinsing—is governed primarily by changes in the surface coverage and interfacial uniformity of the SAM. Specifically, K₂CO₃-mediated deprotonation promotes stronger anchoring of 2PACz on the ITO surface, resulting in a more continuous and uniform SAM with higher surface coverage, which manifests as a deeper WF prior to solvent exposure. Upon DMF rinsing, partial desorption of weakly bound molecules reduces the coverage factor and shifts the measured WF toward that of bare ITO; this effect is pronounced for pristine 2PACz, whereas 2PACz-K retains a relatively stable WF owing to its enhanced interfacial anchoring.

Building on this stabilized interfacial electronic environment, valence band maximum (VBM), conduction band minimum (CBM), and Fermi level (E_F) positions were determined using UPS and optical bandgap data (Figures 2g and S6-S7). After DMF rinsing, ITO/2PACz displayed downward band bending and a large offset ($\Delta E_h = 0.29$ eV) between the VBM of



the perovskite and the highest occupied molecular orbital (HOMO) of ITO/2PACz, forming a barrier for hole extraction.³ In contrast, ITO/2PACz-K exhibited upward band bending with smaller offset ($\Delta E_h = 0.17$ eV), reflecting improved interfacial energetics and a more favorable energy cascade for hole transfer. This alignment optimization, sustained even after solvent exposure, evidences the ability of 2PACz-K to preserve both structural and electronic integrity under realistic processing conditions.

Collectively, these results confirm that K_2CO_3 -mediated deprotonation transforms the SAM into a solvent-resistant interface that maintains chemical integrity, electronic uniformity, and favorable energy level alignment during perovskite processing.

Building on the enhanced interfacial robustness and optimized energy alignment provided by 2PACz-K, the influence of interfacial chemistry on the growth of the overlying perovskite film was further examined. XPS measurements after DMF rinsing show that the K-related signal remains detectable on the ITO/2PACz-K substrate (Figure S8), indicating that potassium species are not completely removed during processing and can persist during subsequent perovskite deposition. To examine the vertical spatial distribution of these potassium species after perovskite crystallization, depth-resolved time-of-flight secondary ion mass spectrometry (TOF-SIMS) analysis was performed (Figure S9). While no detectable K^+ signal was observed for pristine ITO/2PACz/perovskite samples, a clear K^+ signal is detected in ITO/2PACz-K/perovskite structures after perovskite deposition. Notably, the K^+ signal extends across the perovskite region in the depth profile rather than being confined exclusively to the ITO/SAM interface, indicating partial presence of potassium species within the perovskite layer. Because TOF-SIMS depth profiles provide a vertically averaged and semi-quantitative measure, this analysis alone does not allow determination of whether potassium species preferentially reside at grain boundaries, act as bulk defect passivators, or influence the perovskite primarily through electrostatic or chemical interactions at the buried interface. Accordingly, the discussion in this section focuses on the spatial distribution of potassium species and the resulting film growth behavior, while their implications for device operation are examined separately.

Under this stabilized interfacial condition, the structural evolution of the perovskite film is systematically modified. X-ray diffraction (XRD) patterns revealed narrower full widths at half maximum (FWHM) of the (100), (110), and (200) diffraction peaks for films grown on ITO/2PACz-K compared with those on ITO/2PACz (Figure S10), consistent with enhanced crystallinity and improved crystal coherence. Scanning electron microscopy (SEM) images further revealed enlarged grain sizes and a more uniform buried interface for perovskite films



on ITO/2PACz-K (Figure S11), suggesting that a robust and well-anchored SAM promotes uniform nucleation and continuous coverage during crystallization.

The improved structural quality is further reflected in the optoelectronic properties of the perovskite film. The perovskite film grown on ITO/2PACz-K exhibits stronger steady-state photoluminescence (PL) intensity than its 2PACz counterpart (Figure S12), suggesting reduced non-radiative recombination losses under this substrate configuration, where interfacial recombination pathways are typically dominant. Grazing incidence XRD (GIXRD) analysis further indicates that the residual tensile strain in the perovskite film is substantially relaxed when grown on 2PACz-K (Figure S13 and Supplementary Note 3).²⁵ This strain relaxation is consistent with a more strongly coupled buried interface enabled by deprotonated phosphonates, which can provide a more stable interfacial environment during perovskite crystallization.

Time-dependent PL spectra under continuous 1-sun illumination reveal that the perovskite film on ITO/2PACz exhibited a pronounced red shift and spectral broadening associated with light-induced phase segregation (Figure S14a). In contrast, the perovskite film on ITO/2PACz-K maintains a comparable stable emission peak, shifting only slightly from 655 to 659 nm after 20 minutes of illumination (Figure S14b). These observations are consistent with improved crystallization and reduced residual strain enabled by the chemically stabilized buried interface. These effects are consistent with the observed suppression of light-induced phase segregation and are expected to be beneficial for the operational stability of the WBG perovskite layer, as discussed in the following device analysis.^{26,27}

The structural and optoelectronic improvements imparted by 2PACz-K were next evaluated at the device level using WBG PSCs. To evaluate the impact of the modified HSL on device performance, WBG PSCs were fabricated with the configuration ITO/HSL/WBG perovskite/propane-1,3-diammonium iodide (PDAI₂)/C₆₀/SnO₂/Ag (**Figure 3a**). The current density-voltage (*J-V*) characteristics of the devices based on 2PACz and 2PACz-K are compared in Figure 3b, and the corresponding photovoltaic parameters are summarized in Table S6. The 2PACz-K device achieved a higher PCE of 18.25% with V_{OC} of 1.366 V and a fill factor (*FF*) of 83.10%. The hysteresis index was reduced from 7.01% (2PACz) to 4.66% (2PACz-K), consistent with the mitigated lattice strain and reduced defect density in the perovskite layer.²⁸

The integrated photocurrent density values obtained from external quantum efficiency (EQE) spectra were consistent with those from *J-V* measurements (Figure 3c), confirming the reliability of device data. Statistical analysis across 40 devices demonstrated not only higher



average efficiency but also improved reproducibility for the 2PACz-K series (Figures 3d and S15). The stabilized power output (SPO) at maximum power point (MPP) measured for 1000 s under AM 1.5G illumination reached 17.08% for the 2PACz-K device, compared with 15.62% for its 2PACz counterpart (Figure S16). Notably, the FF of 2PACz-K devices reached 85.15% (Figure S17), and $V_{OC} \times FF$ approached $\sim 81\%$ of the S-Q limit for 1.84 eV WBG PSCs, ranking among the highest reported for POTSCs (Figure 3e and Table S7).

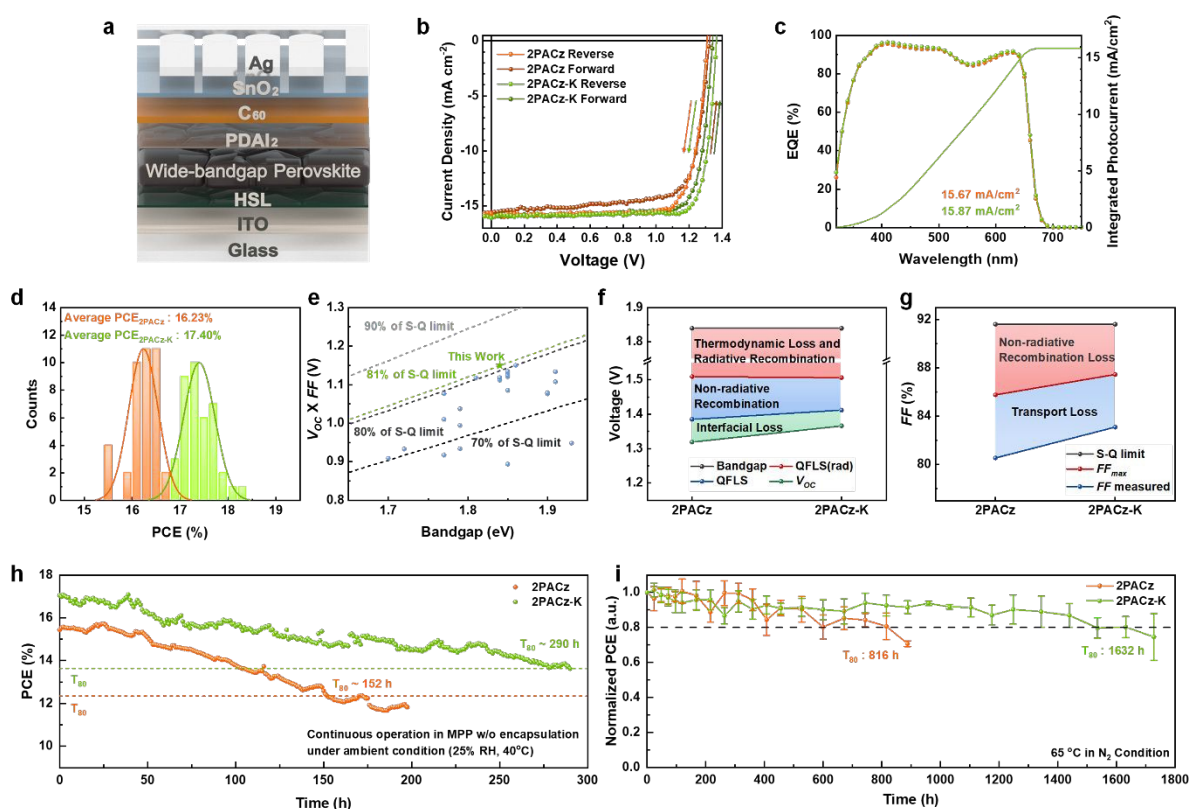


Figure 3. (a) Device structure of WBG PSCs. (b) J - V curves at forward and reverse scan of champion WBG PSCs with 2PACz and 2PACz-K. (c) EQE spectra of WBG PSCs with 2PACz and 2PACz-K. (d) PCE distribution histogram of WBG PSCs. (e) Comparison of $V_{OC} \times FF$ of our WBG PSCs based on 2PACz-K with $E_g \sim 1.84$ eV with those of the previously reported WBG perovskites for POTSCs. (f) V_{OC} loss analysis and (g) FF loss analysis of WBG PSCs. (h) Operational stability of encapsulated WBG PSCs at continuous output at MPP in ambient condition (25% RH, 40°C) under 100 mW cm⁻². (i) Thermal stability of unencapsulated WBG PSCs under 65°C in N₂ atmosphere.

To elucidate the origin of the enhanced photovoltaic performance, transient photocurrent (TPC) and transient photovoltage (TPV) analyses were performed (Figure S18). The 2PACz-

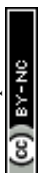


K devices exhibited a shorter TPC decay time ($0.73 \mu\text{s}$ vs. $0.91 \mu\text{s}$) and a longer TPV lifetime ($12.15 \mu\text{s}$ vs. $5.23 \mu\text{s}$), indicating more efficient charge extraction and suppressed recombination. This was further supported by the larger recombination resistance (16103Ω vs. 7866Ω) in electrochemical impedance spectroscopy (EIS) (Figure S19). The higher slope ($\alpha = 0.980$) in the light-intensity-dependent J_{SC} measurements also indicated the lowest charge recombination and the lowest photo-induced leakage current under operating conditions (Figure S20).³ In addition, dark J - V measurements showed a lower low-bias dark current for the 2PACz-K device compared to the 2PACz device, corroborating the suppression of shunt-related leakage paths (Figure S21).

Capacitance-voltage (C - V) measurements and Mott-Schottky plots revealed an increased built-in potential (V_{bi}) for 2PACz-K devices (1.11 V vs. 1.04 V) (Figure S22), suggesting enhanced internal electric field for charge separation. To quantify the V_{OC} improvements, the total V_{OC} loss was deconvoluted into three parts: thermodynamics and radiative recombination losses, non-radiative recombination loss, and interfacial loss (Figure 3f). A detailed breakdown of the V_{OC} losses is provided in Supplementary Note 4, Figure S23, and Table S8. As expected, the thermodynamic/radiative recombination loss was identical owing to the same optical bandgap (1.84 eV).²⁹ The non-radiative recombination loss derived from the photoluminescence quantum yield (PLQY) was reduced from 124 mV (2PACz) to 94 mV (2PACz-K) (Figure S24), while interfacial loss decreased from 66 mV to 46 mV . Together, these factors account for the higher V_{OC} of 1.366 V in the 2PACz-K devices.

The ideality factors (n) extracted from light-intensity-dependent V_{OC} measurements decreased from 1.69 to 1.48 (Figure S25), indicating a reduction in trap-assisted recombination.³⁰ Based on these parameters, the FF loss of the WBG PSCs was subsequently analyzed (Supplementary Note 5). Because both devices show the identical optical bandgap of 1.84 eV , their S-Q limited FF is the same (91.62%).³¹ The FF_{max} was calculated to be 87.46% for 2PACz-K and 85.77% for 2PACz. The difference between FF_{max} and the experimentally measured FF corresponds to transport-induced FF losses of 4.36% for 2PACz-K and 5.23% for 2PACz, respectively (Figure 3g). These improvements confirm that the introduction of 2PACz-K facilitates efficient charge extraction and reduces interfacial losses, yielding devices that are both higher-performing and more stable.

Furthermore, space-charge-limited current (SCLC) measurements on hole-only devices (ITO/HSL/perovskite/poly[bis(4-phenyl)(2,4,6-trimethylphenyl)amine] (PTAA)/Au) showed



a lower hole trap density for 2PACz-K compared with to 2PACz ($2.02 \times 10^{16} \text{ cm}^{-3}$ vs. $2.42 \times 10^{16} \text{ cm}^{-3}$), corroborating the improvements in both V_{OC} and FF (Figure S26).

Finally, operational stability tests demonstrated that encapsulated 2PACz-K devices retained 80% of their initial PCE after 290 h of continuous MPP tracking under ambient conditions, while unencapsulated devices maintained 80% of their initial PCE after 1632 h of thermal aging at 65°C in N_2 atmosphere (Figures 3h-i and S27-S28). These results underscore the contribution of the chemically robust HSL in ensuring durable interfacial contact and stable device operation under realistic conditions. Although both devices exhibit a similar degradation behavior during MPP tracking, the substantially prolonged operational lifetime of the 2PACz-K device reflects enhanced robustness of the buried interface. Importantly, analysis of the MPP operating parameters (Figure S27) shows that the operating voltage (V_{mpp}) remains stable throughout the measurement and that the 2PACz-K device consistently operates at a higher absolute V_{mpp} than the 2PACz device, indicating that the interfacial voltage benefit introduced by the deprotonated SAM is preserved during long-term operation. In contrast, the gradual power decay is dominated by current-related degradation, consistent with intrinsic instability pathways of wide-bandgap perovskite absorbers under illumination. Depth-resolved TOF-SIMS measurements before and after prolonged light soaking and thermal stress show no pronounced vertical redistribution of the K^+ signal (Figures S9b and S29), suggesting that potassium migration is unlikely to be the dominant stability-limiting factor under the tested conditions.

To extend the insights gained from single-junction WBG PSCs to tandem configurations, monolithic POTSCs were fabricated with the structure ITO/2PACz-K/WBG perovskite/PDAI₂/C₆₀/SnO₂/Au/MoO₃/narrow-bandgap (NBG) organic/C₆₀/bathocuproine (BCP)/Ag (Figure 4a). A cross-sectional SEM image of the fabricated tandem device confirmed the well-defined multilayer structure with a sharp perovskite/organic interface (Figure S30). The organic rear sub-cell employed a ternary PM6:BTP-eC9:L8-BO blend that enables high near-infrared (NIR) absorption and efficient current matching with the WBG perovskite front sub-cell. The organic sub-cell exhibited a PCE of 16.30%, with V_{OC} of 0.873 V, J_{SC} of 26.91 mA cm⁻² (Figure 4b and Table S9). Its high EQE, reaching ~85% in the NIR region (Figure S31), confirms efficient photocurrent harvesting and facilitates balanced current generation within the tandem stack.

View Article Online
DOI: 10.1039/D5EE07006F



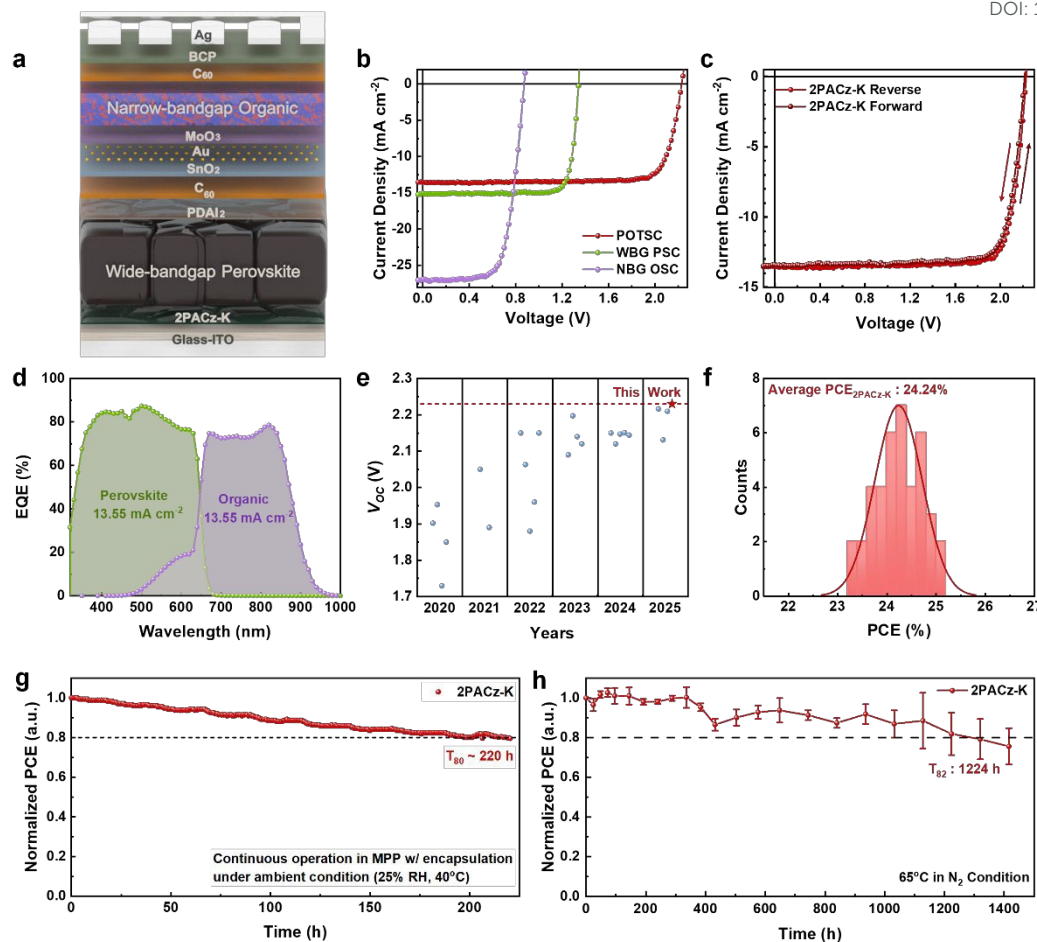


Figure 4. (a) Device structure of POTSCs with 2PACz-K. (b) J - V curves of champion perovskite sub-cell, organic sub-cell, and POTSCs at reverse scan. (c) J - V curves of POTSCs at forward and reverse scan, and (d) EQE spectra of two sub-cells in POTSCs with 2PACz-K. (e) Comparison of V_{OC} of our POTSCs with that of previously reported p-i-n-structured POTSCs. (f) PCE distribution histogram and (g) Operational stability of encapsulated POTSCs at continuous output at MPP in ambient condition (25% RH, 40°C) under 100 mW cm⁻². (h) Thermal stability of unencapsulated POTSCs with 2PACz-K under 65°C in N₂ atmosphere.

The tandem devices based on pristine 2PACz reached a PCE of 23.20% (Table S10). Upon replacement with 2PACz-K, the champion POTSC achieved a PCE of 25.10% (reverse scan) with a V_{OC} of 2.230 V, J_{SC} of 13.54 mA cm⁻², and FF of 83.15% (Figure 4b and Table S9). The hysteresis index was reduced from 4.68% (2PACz) to 3.71% (2PACz-K), consistent with the reduced strain and suppressed phase segregation observed in the single-junction devices (Figure 4c and Table S10).



The EQE spectra of both sub-cells confirmed proper current matching and yielded integrated J_{SC} values consistent with the $J-V$ measurements (Figure 4d). Notably, the V_{OC} of 2.230 V represents one of the highest reported among p-i-n structured POTSCs, confirming that the mixed deprotonated states in 2PACz-K effectively minimize interfacial losses (Figure 4e and Table S11). Statistical analysis of 40 independent devices demonstrated a narrow PCE distribution and high reproducibility (Figures 4f and S32), while stabilized power output (SPO) measurements at MPP yielded a steady-state PCE of 22.74% (Figure S33). To further validate device reliability, a certified efficiency measurement confirmed a PCE of 24.00% for the 2PACz-K POTSCs (Figure S34).

The 2PACz-K-based POTSCs also exhibited remarkable operational durability, retaining 80% of their initial PCE after 220 h of continuous MPP tracking under 1-sun illumination in ambient air (Figures 4g and S35). In thermal aging tests at 65°C in N_2 atmosphere, unencapsulated devices maintained 82% of their initial efficiency after 1224 h (Figures 4h and S36). These results underscore that the robust interfacial binding and enhanced solvent resistance of 2PACz-K are key to the long-term operational stability of monolithic POTSCs.

Encouraged by the exceptional operational stability of 2PACz-K-based POTSCs, the same interfacial strategy was extended to photoelectrochemical devices for solar-to-hydrogen conversion. Notably, this work represents the first demonstration of a transparent, metal-free POT-PEC in which an EQE spectrum was successfully measured, enabling quantitative validation of photocurrent generation in a tandem photocathode. The device configuration and corresponding water-splitting system are illustrated in **Figure 5a**. Because electrolyte penetration is a major degradation pathway in photoelectrochemical operation, hydrophobic organic layers alone are insufficient to provide long-term protection, therefore, additional inorganic overlayers are often required to enhance durability.^{9,32,33} Accordingly, an atomic layer deposition (ALD)- TiO_x overlayer was introduced on top of the organic sub-cell. The resulting dual protective stacks—comprising the organic layer and the TiO_x overlayer—effectively suppresses electrolyte ingress. After establishing the protective architecture, a RuO_2 catalyst was deposited by a photo-assisted electrodeposition method.³⁴

Comparative measurements revealed that the TiO_x overlayer reduced J_{SC} in POTSCs because of the intrinsic resistivity of the metal oxide (Figure S37 and Table S12). When the TiO_x layer becomes sufficiently resistive and charge extraction becomes transport-limited, a finite voltage drop can develop across the overlayer even under short-circuit conditions, which enhances charge accumulation and interfacial recombination and thereby reduces the collected



J_{SC} .³⁵ In contrast, POT-PECs incorporating TiO_x overlayer exhibited enhanced J_{ph} , attributed to the uniform, pinhole-free coverage that blocks electrolyte penetration and enhanced electron selectivity (Figures 5b and S38a-b).³² The optimized POT-PEC with 2PACz-K delivered a stable J_{ph} of 7.1 mA cm^{-2} and a V_{ph} of 2.16 V in 0.5 M KPi electrolyte (pH 7.0). The EQE spectrum recorded at 0 V_{RHE} (Figure 5c) closely resembled that of the corresponding POTSCs, confirming proper operation of both sub-cells. The integrated J_{ph} was slightly reduced due to partial attenuation of the bias light while passing through the aqueous electrolyte, consistent with previous reports.³⁶ Importantly, this constitutes the first validated EQE measurement of a tandem photocathode, providing a quantitative benchmark for photocurrent generation in tandem PECs.

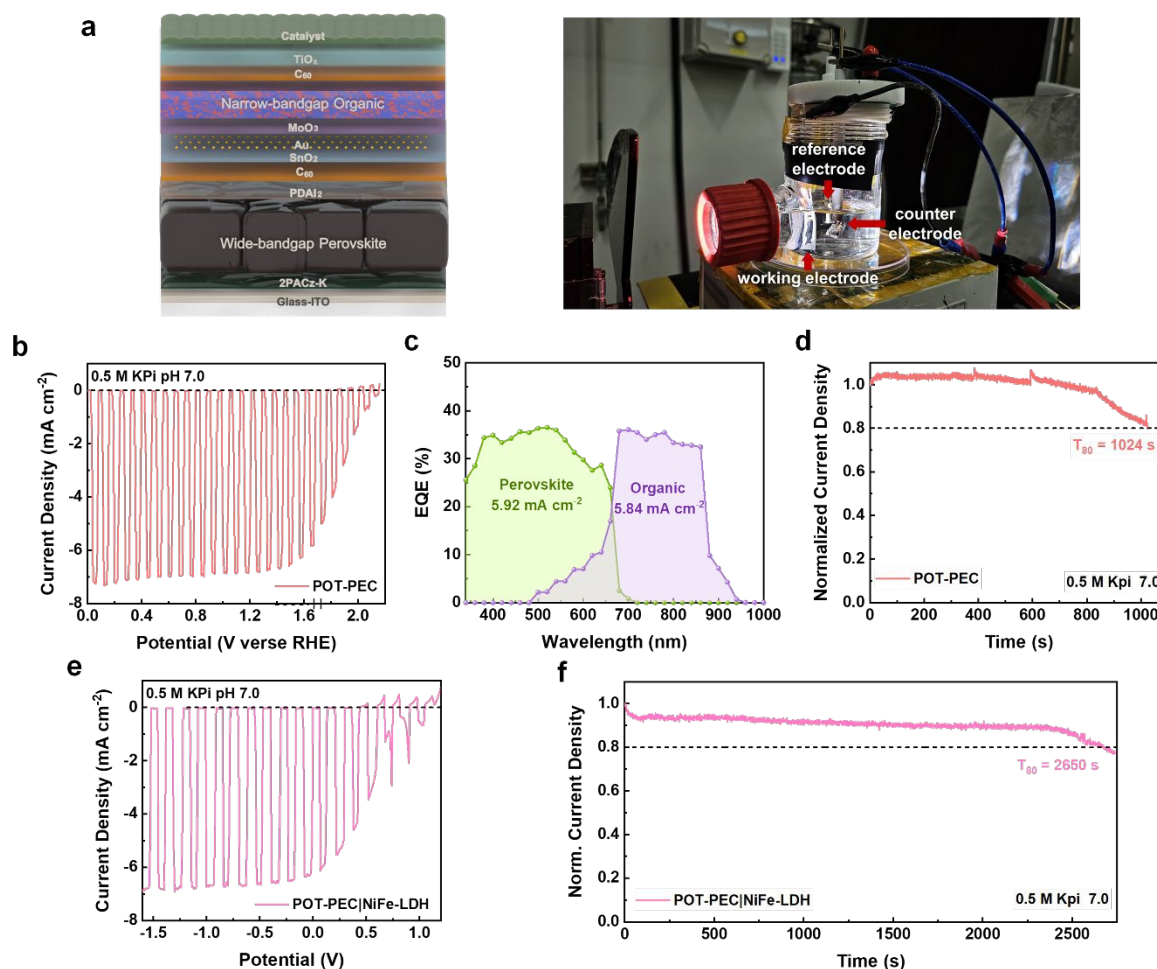


Figure 5. (a) Schematic image of POT-PEC structure and photograph of photoelectrochemical system. (b) LSV curve and (c) EQE measurement of POT-PEC in 0.5 M KPi . (d) CA measurement of POT-PEC at 0.1 V_{RHE} . (e) LSV curve and (f) CA measurement POT-PEC with NiFe-LDH operated in two electrode configurations.



As demonstrated in Figure 5d, the POT-PEC maintained a T_{80} lifetime of 1024 s, whereas thinner ALD- TiO_x film failed within few minutes (Figure S38c). These results indicate that the 2PACz-K-based interface, in combination with the conformal TiO_x overlayer, provides effective protection against electrolyte penetration and enables stable short-term operation in aqueous environments. Furthermore, to assess the solar-to-hydrogen conversion efficiency, we operated the POT-PEC in a two-electrode configuration. To reduce the anodic overpotential, the Pt was replaced with a NiFe-LDH oxygen-evolution anode. As shown in Figure 5e, the two-electrode configuration is consistent with the trend observed in the three-electrode measurements (Figure 5b), and the device reaches a current density of 6.25 mA cm^{-2} at 0 V (short-circuit) in 0.5 M KPi (pH 7.0). The corresponding solar-to-hydrogen (STH) conversion efficiency is estimated to be up to 7.7%, assuming a Faradaic efficiency of 100 %. In addition, chronoamperometry measured at 0 V demonstrates sustained bias-free operation with a T_{80} lifetime of 2650 s (Figure 5f).

Overall, this work demonstrates a unified interface engineering strategy that enhances the efficiency and durability of POTSCs and extends their applicability to transparent, metal-free photocathode for solar-driven hydrogen generation. By chemically stabilizing the TCO/SAM interface through a solution-based, low-temperature deprotonation process that enables uniform and robust SAM formation, this strategy is intrinsically independent of absorber configuration and device geometry. As a result, the same interfacial concept provides a foundation not only for bias-free CO_2 reduction using tandem photocathode-photoanode systems, but also, in principle, for mechanically compliant and scalable photovoltaic architectures beyond rigid, small-area devices.

Conclusion

The incorporation of K_2CO_3 drives stepwise deprotonation of 2PACz, producing mixed mono- and di-deprotonated species (2PACz-K) that form strong P-O-M coordination with ITO. This interfacial chemistry enables the formation of uniform and solvent-resistant SAMs, ensuring stable energy-level alignment and defect suppression during perovskite deposition. As a result, WBG PSCs incorporating 2PACz-K achieved high V_{OC} (1.366 V) and FF (83.10%), leading to a PCE of 18.25%. When implemented in monolithic POTSCs, the improved interfacial robustness translated to a champion efficiency of 25.10% and a certified 24.00%, with excellent operation stability in both light and thermal stress conditions. Extending this strategy to photoelectrochemical systems, the first transparent, metal-free POT-PEC



demonstrated stable operation and EQE-validated photocurrent generation in neutral electrolyte, delivering a V_{ph} of 2.16 V and achieving STH conversion efficiency of 7.7%. These findings highlight 2PACz-K as a versatile interfacial material that bridges solid-state photovoltaics and solar-driven chemical conversion, offering a promising foundation for scalable and durable solar-fuel systems.

Author Contributions

J.G.S., H.K., and W.L. equally contributed to this work. J.Y.K. and D.S.K. supervised the work. J.G.S., H.K., W.L., and J.Y.K. wrote the manuscript. J.G.S. and H.K. carried out the solar cell fabrication and characterizations. W.L. carried out the photocathode fabrication and characterizations. S.J.G. carried out EIS measurements. H.K. carried out SEM, and PL measurements. S.P., H.L., and S.C. carried out KPFM, TPV, and TPC measurements. J.W and S.-J.S. carried out DFT calculations. J.R. carried XPS and UPS measurements. J.M.H. and H.Y.W. carried out PLQY measurements. J.S. carried out XRD measurements. W.L. carried out UV-vis absorption measurements.

Conflicts of interest

The authors declare no competing interests.

Acknowledgments

We thank Dr. Jin Hyun Kim (Postdoctoral researcher in Prof. Michael Grätzel's group) for his helpful suggestions regarding the development of the ALD-TiO_x deposition process. This work was supported by the National Research Foundation of Korea (NRF) grant funded by the Korea government (MSIT) (RS-2024-00346361, RS-2024-00429694).



References

1. National Renewable Energy Laboratory (NREL), Best Research-Cell Efficiency Chart, 2025, <https://www.nrel.gov/pv/cell-efficiency.html> (accessed: October 2025).
2. K. Wang, L. Zheng, Y. Hou, A. Nozariasbmarz, B. Poudel, J. Yoon, T. Ye, D. Yang, A. V. Pogrebnyakov, V. Gopalan and S. Priya, *Joule*, 2022, **6**, 756–771.
3. J. G. Son, S. Ameen, J. Roe, S. Park, J. Seo, J. Kim, A. B. Faheem, H.-e. Koo, S. O. Oh, Y. Jo, J. W. Kim, Y. Lee, Y. S. Shin, H. Jang, D. Lee, S. Hur, K.-K. Lee, S. Cho, D. S. Kim, J. Y. Kim and B. Kim, *Adv. Energy Mater.*, 2025, **15**, 2404092.
4. Y. Han, J. Fu, Z. Ren, J. Yu, Q. Liang, Z. Xu, X. Xie, D. Li, R. Ma, M. Cao, Y. Sun, C. Yang, J. He, X. Chang, K. Liu, P. W. K. Fong, J. Huang, H. Liu, Z. Liu, D. Xu, L. Cheng, J. Zhang, G. Yang, X. Lu, Y. Zhu, Q. Tai, Q. Lin, H. Hu, Y. Yang and G. Li, *Nat. Energy*, 2025, **10**, 513–525.
5. Y. An, N. Zhang, Q. Liu, W. Jiang, G. Du, D. Chen, M. Liu, X. Huang, T. Lei, Q. Qiu, F. R. Lin, X. C. Zeng, A. K. Y. Jen and H.-L. Yip, *Nat. Commun.*, 2025, **16**, 2759.
6. S. Wu, Y. Yan, J. Yin, K. Jiang, F. Li, Z. Zeng, S.-W. Tsang and A. K. Y. Jen, *Nat. Energy*, 2024, **9**, 411–421.
7. D. Zhao, C. Chen, C. Wang, M. M. Junda, Z. Song, C. R. Grice, Y. Yu, C. Li, B. Subedi, N. J. Podraza, X. Zhao, G. Fang, R.-G. Xiong, K. Zhu and Y. Yan, *Nat. Energy*, 2018, **3**, 1093–1100.
8. F. Hao, C. C. Stoumpos, R. P. H. Chang and M. G. Kanatzidis, *J. Am. Chem. Soc.*, 2014, **136**, 8094–8099.
9. B. Wu, T. Wang, B. Liu, H. Li, Y. Wang, S. Wang, L. Zhang, S. Jiang, C. Pei and J. Gong, *Nat. Commun.*, 2022, **13**, 4460.
10. Z. Wei, Q. Zhou, X. Niu, S. Liu, Z. Dong, H. Liang, J. Chen, Z. Shi, X. Wang, Z. Jia, X. Guo, R. Guo, X. Meng, Y.-D. Wang, N. Li, Z. Xu, Z. Li, A. G. Aberle, X. Yin and Y. Hou, *Energy Environ. Sci.*, 2025, **18**, 1847–1855.
11. R. He, Z. Yi, Y. Luo, J. Luo, Q. Wei, H. Lai, H. Huang, B. Zou, G. Cui, W. Wang, C. Xiao, S. Ren, C. Chen, C. Wang, G. Xing, F. Fu and D. Zhao, *Adv. Sci.*, 2022, **9**, 2203210.
12. G. Wang, J. Zheng, W. Duan, J. Yang, M. A. Mahmud, Q. Lian, S. Tang, C. Liao, J. Bing, J. Yi, T. L. Leung, X. Cui, H. Chen, F. Jiang, Y. Huang, A. Lambertz, M. Jankovec, M. Topič, S. Bremner, Y.-Z. Zhang, C. Cheng, K. Ding and A. Ho-Baillie, *Joule*, 2023, **7**, 2583–2594.
13. Z. Yi, W. Wang, R. He, J. Zhu, W. Jiao, Y. Luo, Y. Xu, Y. Wang, Z. Zeng, K. Wei, J. Zhang, S.-W. Tsang, C. Chen, W. Tang and D. Zhao, *Energy Environ. Sci.*, 2024, **17**, 202–209.
14. S. Fu, N. Sun, H. Chen, Y. Li, Y. Li, X. Zhu, B. Feng, X. Guo, C. Yao, W. Zhang, X. Li and J. Fang, *Energy Environ. Sci.*, 2025, **18**, 3305–3312.
15. H. Tang, Z. Shen, Y. Shen, G. Yan, Y. Wang, Q. Han and L. Han, *Science*, 2024, **383**, 1236–1240.
16. A. Al-Ashouri, A. Magomedov, M. Ross, M. Jost, M. Talaikis, G. Chistiakova, T. Bertram, J. A. Márquez, E. Köhnen, E. Kasparavicius, S. Levenco, L. Gil-Escrig, C.



- J. Hages, R. Schlatmann, B. Rech, T. Malinauskas, T. Unold, C. A. Kaufmann, L. Korte, G. Niaura, V. Getautis and S. Albrecht, *Energy Environ. Sci.*, 2019, **12**, 3356–3369.
17. R. He, W. Wang, Z. Yi, F. Lang, C. Chen, J. Luo, J. Zhu, J. Thiesbrummel, S. Shah, K. Wei, Y. Luo, C. Wang, H. Lai, H. Huang, J. Zhou, B. Zou, X. Yin, S. Ren, X. Hao, L. Wu, J. Zhang, J. Zhang, M. Stolterfoht, F. Fu, W. Tang and D. Zhao, *Nature*, 2023, **618**, 80–86.
18. R. Azmi, D. S. Utomo, B. Vishal, S. Zhumagali, P. Dally, A. M. Risqi, A. Prasetio, E. Ugur, F. Cao, I. F. Imran, A. A. Said, A. R. Pininti, A. S. Subbiah, E. Aydin, C. Xiao, S. I. Seok and S. De Wolf, *Nature*, 2024, **628**, 93–98.
19. W. Yang, Y. Lin, W. Zhu, F. Du, J. Liu, Y. Ren, H. Wang, J. Liao, D. Yu, G. Fang, M. Li, R. Zhang, S. Yang and C. Liang, *Adv. Mater.*, 2025, **37**, 2502865.
20. C. Li, Y. Chen, Y. Li, L. Gong, Z. Yuan, L. Liang, J. Chen, P. Ganesan, Y. Zhang, J. Ma and P. Gao, *Angew. Chem., Int. Ed.*, 2025, **64**, e202420585.
21. H. Guo, G. Yang, A. Zhang, H. Jiang, H. Lu and Z. Bo, *Small*, 2025, **21**, e04509.
22. H. Tang, L. Yang, P. Li, J. Li, Y. Yang, R. Xu, Y. Sun, W. Cai, J. Wang, J. Xu, C. Zuo, L. Ding, Z. Wu and H. Dong, *Adv. Funct. Mater.*, 2025, DOI: <https://doi.org/10.1002/adfm.202516652>, e16652.
23. X. Hu, C. Liu, Z. Zhang, X. F. Jiang, J. Garcia, C. Sheehan, L. Shui, S. Priya, G. Zhou, S. Zhang and K. Wang, *Adv. Sci.*, 2020, **7**, 2001285.
24. M. Liu, L. Bi, W. Jiang, Z. Zeng, S. W. Tsang, F. R. Lin and A. K. Jen, *Adv. Mater.*, 2023, **35**, 2304415.
25. H. Jang, H. Y. Lim, C. B. Park, J. Seo, J. G. Son, T. Song, J. Lee, Y. S. Shin, J. Roe, S. K. Kwak, D. S. Kim and J. Y. Kim, *J. Mater. Chem. A*, 2023, **11**, 10605–10611.
26. D. J. Kubicki, D. Prochowicz, A. Hofstetter, S. M. Zakeeruddin, M. Grätzel and L. Emsley, *J. Am. Chem. Soc.*, 2017, **139**, 14173–14180.
27. Z. Fang, T. Nie, S. Liu and J. Ding, *Adv. Funct. Mater.*, 2024, **34**, 2404402.
28. W. Meng, K. Zhang, A. Osvet, J. Zhang, W. Gruber, K. Forberich, B. Meyer, W. Heiss, T. Unruh, N. Li and C. J. Brabec, *Joule*, 2022, **6**, 458–475.
29. A. Sun, C. Tian, R. Zhuang, C. Chen, Y. Zheng, X. Wu, C. Tang, Y. Liu, Z. Li, B. Ouyang, J. Du, Z. Li, J. Cai, J. Chen, X. Wu, Y. Hua and C. C. Chen, *Adv. Energy Mater.*, 2024, **14**, 2303941.
30. J. Roe, J. G. Son, S. Park, J. Seo, T. Song, J. Kim, S. O. Oh, Y. Jo, Y. Lee, Y. S. Shin, H. Jang, D. Lee, D. Yuk, J. G. Seol, Y. S. Kim, S. Cho, D. S. Kim and J. Y. Kim, *ACS Nano*, 2024, **18**, 24306–24316.
31. H. Fujiwara, in *Wiley-VCH*, 2022, DOI: <https://doi.org/10.1002/9783527825851>, ch. Appendix B: Numerical Values of Shockley–Queisser Limit, pp. 563–565.
32. L. Steier, S. Bellani, H. C. Rojas, L. Pan, M. Laitinen, T. Sajavaara, F. Di Fonzo, M. Grätzel, M. R. Antognazza and M. T. Mayer, *Sustain. Energy Fuels*, 2017, **1**, 1915–1920.
33. K.-M. Lee, C.-C. Chen, L.-C. Chen, S. H. Chang, K.-S. Chen, S.-C. Yeh, C.-T. Chen and C.-G. Wu, *Sol. Energy Mater. Sol. Cells*, 2017, **164**, 13–18.
34. S. D. Tilley, M. Schreier, J. Azevedo, M. Stefik and M. Graetzel, *Adv. Funct. Mater.*, 2014, **24**, 303–311.



View Article Online
DOI: 10.1039/D5EE07006F

35. A. Sławek, Z. Starowicz and M. Lipiński, *Materials*, 2021, **14**, 3295.
36. H. Döscher, J. F. Geisz, T. G. Deutsch and J. A. Turner, *Energy Environ. Sci.*, 2014, **7**, 2951–2956.



Data Availability Statement (DAS)

All data supporting the results of this study are included in the manuscript and its Supplementary Information files (ESI).

